TREVR: A general $O\left(N \log^2 N\right)$ radiative transfer algorithm

J. J. Grond, R. M. Woods, J. Wadsley * and H. M. P. Couchman
Department of Physics and Astronomy, McMaster University, Hamilton, Ontario L8S 4M1, Canada

ABSTRACT

We present TREVR (Tree-based Reverse Ray Tracing), a general algorithm for computing the radiation field, including absorption, in astrophysical simulations. TREVR is designed to handle large numbers of sources and absorbers. TREVR is based on a *tree* data structure and is thus suited to codes that use trees for their gravity or hydrodynamics solvers (e.g. Adaptive Mesh Refinement). It achieves computational speed while maintaining a specified accuracy via controlled lowering of resolution of both sources and rays from each source. TREVR computes the radiation field in $O(N \log N_{\mathrm{source}})$ time without absorption and $O(N \log N_{\mathrm{source}} \log N)$ time with absorption. These scalings arise from merging sources of radiation according to an opening angle criterion and walking the tree structure to trace a ray to a depth that gives the chosen accuracy for absorption. The absorption depth refinement criterion is unique to TREVR. We provide a suite of tests demonstrating the algorithm's ability to accurately compute fluxes, ionization fronts and shadows.

Key words: radiative transfer – methods: numerical

1 INTRODUCTION

Radiation is arguably the most important physical phenomena to the field of astrophysics. Almost all of the information we receive from outer space comes in the form of photons we detect on or around earth. Understanding the process of radiative transfer (RT) is key in interpreting this information, as the photons are affected by the medium they travel through on their way to our telescopes and detectors. Interactions between photons and the medium do not only affect the photons themselves but the matter as well. Photons and baryons exchange energy and momentum, driving both heating and cooling. This also affects excitation and ionization states and thus determines the chemical and thermodynamic properties of the gas. Thus radiation is a key in many of the astrophysical systems and processes we study.

On galaxy scales, a central question is how feedback mechanisms affect star and galaxy formation. Stellar feedback comes in the form of photoionization by ultraviolet (UV) radiation, stellar winds and supernovae (Leitherer et al. 1999), the latter of which has been a main focus in simulations in previous years (Agertz et al. 2013). It is important to note that even though supernovae might be spectacularly powerful events, ionizing radiative output from stellar populations contributes two orders of magnitude more energy at early times and about 50 times more energy over the course of a stellar population's lifetime. This is made evident
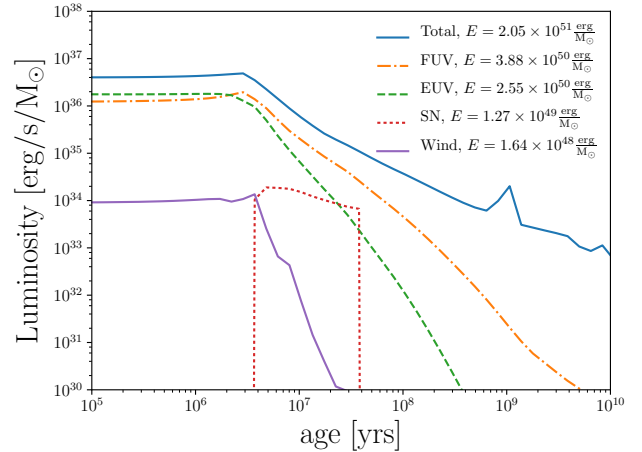
Figure 1. Luminosity per solar mass as a function of time for a stellar population having a Chabrier initial mass function (Chabrier 2003).

in Figure 1, a plot of luminosity output per solar mass as a function of time from stellar populations created via output from the stellar evolution code Starburst99 (Leitherer et al. 1999).

However, the way in which this massive output of UV radiation is deposited and consequently affects the interstellar medium (ISM) is still unclear. Attempts at numerically

* E-mail: wadsley@mcmaster.ca

exploring these affects without the use of a full radiative transfer method have produced conflicting results. Simulations done by Gritschneder et al. (2009) and (Walch et al. 2012) suggest that ionizing feed back from large O-type stars before the first supernovae ($< 1 - 3\text{Myr}$) have a significant effect on star formation rate. Whereas Dale et al. (2012) conclude the affects on star formation rate to be small.

With that in mind it may then come as a surprise that RT has been treated poorly in most galaxy scale astrophysical simulations, usually as some imposed uniform background. This is because RT is an intrinsically complex and expensive problem. The complexity of this problem is firstly evident from the full RT equation (e.g. Mihalas & Mihalas 1984),

$$\left[\frac{1}{c}\frac{\partial}{\partial t} + \hat{\mathbf{n}} \cdot \nabla\right] I\left(\mathbf{x}, \hat{\mathbf{n}}, t, \nu\right) = \epsilon\left(\mathbf{x}, \hat{\mathbf{n}}, t, \nu\right) - \alpha\left(\mathbf{x}, \hat{\mathbf{n}}, t, \nu\right) I\left(\mathbf{x}, \hat{\mathbf{n}}, t, \nu\right),$$
$$(1)$$

where I, ϵ and α are the intensity, emissivity and extinction coefficients respectively and all depend on position $\mathbf{x}$, unit direction of light propagation $\hat{\mathbf{n}}$, time t and frequency ν. Apart from being a seven dimensional problem, RT has the highest possible characteristic speed of c, the speed of light. Also, unlike a force at a distance problem such as gravity, RT depends on the properties of the intervening material via the absorption term, α.

Because of this complexity, a naïve numerical solution to the RT problem scales with the number of resolution elements, N, as $O\left(N^{7/3}\right)$ and requires a timestep thousands of times smaller than typical Courant times in astrophysics. This scaling arises due to three contributions. Firstly, a radiation field must be computed at each of the simulation's N resolution elements. Secondly, each resolution element's intensity value is made up of contributions from N_{source} sources of radiation (N_{source} rays of light being computed per resolution element). This leads to a scaling for the total of rays, $N_{\text{ray}} = N \times N_{\text{source}}$, or $O\left(N^2\right)$ assuming the $N_{\text{source}} \sim N$. This fact alone limits brute-force RT methods to only small scale problems, such as ionization by a small handful of massive stars (Howard et al. 2016, 2017). Finally, each ray of light interacts with the medium along its path, which is resolved with $O\left(N^{1/3}\right)$ resolution elements. Thus the computational cost is $O\left(N^{7/3}\right)$. This poor scaling with resolution elements makes it unfeasible to simulate RT alongside gravity and hydrodynamics methods that scale as $O\left(N \log N\right)$ or better. It is evident that much can be gained by reducing the linear dependence on N_{source}, with additional gains from tackling the $N^{1/3}$ cost per ray.

A feasible RT method would have to solve a simplified RT problem. RT methods can be divided into two different categories based on how they treat c in Equation 1. *Evolutionary* methods use a finite c, (which is often reduced from the true speed of light) and thus the partial time derivative remains in Equation 1 and the radiation field is advected or evolved throughout the simulation. The prototypical evolutionary method is flux limited diffusion (Levermore & Pomraning 1981). Modern evolutionary methods include include moment methods like OTVET (Gnedin & Abel 2001) and RAMESE-RT (Rosdahl & Teyssier 2015) as well as photon packet propagation methods like TRAPHIC (Pawlik & Schaye 2008), SPHRAY (Altay et al. 2008) and SimpleX2 (Paardekooper et al. 2010).

On the other hand, *Instantaneous* Methods take the limit where c is infinite and the partial time derivative in Eq. 1 goes to zero and the radiation field can be computed instantaneously as a computational geometry problem. Methods in this category include forward ray tracers such as C^2Ray (Mellema et al. 2006), Moray (Wise & Abel 2011) and Fervent (Baczynski et al. 2015) as well as reverse ray tracers such as TreeCol (Clark et al. 2012) and URCHIN (Altay & Theuns 2013).

Instantaneous methods typically take the form of ray tracers. Ray tracers are the most direct way to go about solving the RT problem. Forward ray tracers trace many rays outward from sources of radiation, similarly to the actual phenomena, in the hope that resolution elements will have sufficiently many rays intersecting them to compute a radiation field. Naïvely, the number of rays per source would be comparable to the number of resolution elements, giving a scaling of $O\left(NN_{\text{source}}N^{1/3}\right)$, as previously noted. However, for forward ray tracing, $O\left(N^{2/3}\right)$ rays per source are typically sufficient to hit every resolution element when extended to the edge of the simulation volume (distance $O\left(N^{1/3}\right)$), so the scaling typically achieved is $O\left(NN_{\text{source}}\right)$.

It is important to note that methods that adaptively split rays (e.g. Healpix (Górski et al. 2005) used in Moray, URCHIN and TreeCol), do not change the overall scaling. For example, a centrally located source requires $6N^{2/3}$ rays to strike all elements in the outer faces of a cubical simulation volume, each with a length $O\left(N^{1/3}\right)$. Even with adaptive ray merging near the source, at least N ray segments are required to intersect each of the N resolution elements. In additon, ray tracers such as Moray rely upon a Monte-Carlo approach to estimate the radiation field and thus require atleast 10 rays to intersect each element, a prefactor to the overall cost. This scaling usually limits forward ray tracers to problems with few sources to avoid $O(N^2)$ like scaling.

Recently there has been some focus on reverse ray tracing methods by Clark et al. (2012) and Altay & Theuns (2013). These particular methods are not general, as they are designed to compute external radiation (e.g. from the post ionization UV background) rather than internal sources of radiation. However, the idea of reverse ray-tracing introduces many advantages relative to forward raytracing. The main difference between forward and reverse ray tracing is that reverse ray tracers trace rays from the resolution elements directly to the sources of radiation. Tracing from the sinks guarantees the density distribution is well sampled near the resolution element as apposed to forward ray tracing where one would have to increase the number of rays per sink to guarantee this type of accuracy. Put simply, radiation is computed exactly where it is needed. This is especially advantageous in adaptive mesh and Lagrangian simulations such as smoothed particle hydrodynamics (SPH) simulations, as low density regions are represented by few resolution elements, and thus extra work is not done to resolve radiation in said regions.

A key benefit to reverse ray tracing is that adaptive time steps dramatically reduce the radiation work as only active resolution elements, N_{sink}, need to be traced to. This active subset can be 100 times smaller on average than N in high-resolution cosmological simulations. Scaling work with the active subset is key for computational efficiency for both

the gravity and hydro solvers for any simulation with a high dynamic range. Thus a naïve reverse ray trace still scales as $O\left(N_{\text{sink}} N_{\text{source}} N^{1/3}\right)$ and many sources present the most significant barrier.

Evolutionary methods are typically based on evolving moments of the radiation field stored at each resolution element. They are insensitive to the number of sources, and scale as $O(N)$ with the number of resolution elements, allowing them to handle large numbers of sources and scattering. Although evolutionary methods can handle both optically thin and thick regimes, they loose directional accuracy in intermediate regimes and suffer from poor directional accuracy in general. This is immediately apparent in shadowing type tests.

Photon packet propagation methods, such as TRAPHIC (Pawlik & Schaye 2008), are an evolutionary approach where directional accuracy is easier to control, in principle. However, the Monte Carlo aspects of how photon packets are propagated introduce significant Poisson noise into their computed radiation field. Added Monte Carlo resampling is shown to reduce this noise but is quite expensive and deteriorates the initially sharp shadowsi, and is typically not used in production runs. TRAPHIC also adds virtual particles (ViPs) to propagate their photon packets in less dense, optically thin regions lacking in SPH particles. TRAPHIC scales linearly with resolution elements, as mentioned before.

A key limitation for moment methods is that the radiation field for every element needs to be computed every step. In addition, the speed of light, even when reduced, is substantially larger than the sound speed and thus many radiation substeps are required compared to the hydro solver. Thus for photon packet propagation methods every photon packet typically hops forward several times for each hydro step. A key outcome is that moment methods cannot take advantage of adaptive timesteps to limit radiation work. Specifically in the case of TRAPHIC, the N is significantly greater than the number of SPH particles including the addition of ViPs. These factors dramatically increase the prefactor on the scaling. None-the-less, moment methods such as TRAPHIC represent an viable approach for large simulations that can handle a variety of regimes of optical depth.

We hope from this introduction to the state of the art in RT methods it is apparent that there is room for improvement, especially in the area of instantaneous methods. Although promising work has been done with reverse ray tracers like TreeCol and URCHIN, a general implementation of one has yet to be developed and published. There is also the problem of scaling with radiation sources in instantaneous methods that reverse ray tracers alone do not solve. Therefore we have developed TREVR, a $O\left(N \log^2 N\right)$ reverse ray tracer designed to solve these problems and fill this niche. In Section 2 we detail the specific RT equations TREVR solves (Subsection 2.1) and the general TREVR algorithm (Subsection 2.2) as well as specifics of our implementation in GASOLINE (Subsection 2.3). In Section 3 we present a suite of tests demonstrating the algorithm's ability to accurately compute fluxes, ionization fronts and shadows in the optically thick and thin regimes. These tests also allow us to explore how TREVR's accuracy criteria predicts error and affects computational cost. The computational cost is bounded and characterized in a general case to substanti-

ate the $O\left(N \log^2 N\right)$ claim made earlier. Finally, in Section 4 we discuss TREVR's strengths and shortcomings and conclude how they enable and constrain the types of problems TREVR can handle. We will also discuss apparent improvements that can be made in the future in this section.

2 METHOD

2.1 Simplifications to the full RT problem

Before describing TREVR, let's first define the simplified version of the classical RT equation the method solves. Since TREVR is an instantaneous method, c is set to infinity eliminating the partial time derivative in 1 leaving us with the instantaneous RT equation,

$$\hat{\mathbf{n}} \cdot \nabla I(\mathbf{x}, \hat{\mathbf{n}}, t, \nu) = \epsilon(\mathbf{x}, \hat{\mathbf{n}}, t, \nu) - \alpha(\mathbf{x}, \hat{\mathbf{n}}, t, \nu) I(\mathbf{x}, \hat{\mathbf{n}}, t, \nu). \quad (2)$$

The emissivity term in the above equation, ϵ, describes a continuous emitting medium. TREVR assumes sources of radiation are continuous, but being a numerical method it needs to represent sources of radiation as discrete resolution elements. In this case ϵ is a sum of delta functions and the solution to the RT equation becomes a linear combination of contributions from all sources of radiation. Also, since we are considering sources one by one we can start using the path length s between a source and resolution element as our integration element

$$\frac{dI}{ds} = -\alpha I. \quad (3)$$

We can then combine the path length and extinction coefficient to solve for intensity by integrating

$$d\tau = \kappa \rho ds, \quad (4)$$

the optical depth, where κ is opacity and ρ is density. This leaves us with

$$\frac{dI}{d\tau} = -I, \quad (5)$$

the final version of the RT problem this method solves. The solution to this equation is

$$I(s) = I(s_0) e^{-\tau(s)}, \quad (6)$$

where $I(s_0)$ is the intensity of the source and $\tau(s)$ is the only quantity to be integrated in our method

$$\tau(s) = \int_{s_0}^{s} \kappa(s) \rho(s) ds. \quad (7)$$

Wadsley: This is a bit out of the blue. You just skipped from one source to all of them without saying you did that. Grond: I'm a bit stuck on this.

We can use the radiation intensity directly in heating, chemistry and ionization functions which are typically a function the total intensity from all radiation sources. We can then take moments of the intensity to obtain useful quantities such as radiation flux

$$\mathbf{F} = \int I \cos\theta d\Omega \hat{\mathbf{n}}, \quad (8)$$

and radiation pressure

$$\mathbf{p} = \frac{1}{c} \int I \cos^2\theta d\Omega \hat{\mathbf{n}}. \quad (9)$$

Wadsley: What is dOmega – where did the integrals come from? Grond: Rybicki and Lightman. Wadsley: It might be clearer if you said, "for point sources the contribution is I delta(theta)" or something like that. Grond: Need some clarification here. Because we assume our sources of radiation to be true point sources, $cos\theta$ = 1. If the angular size of a resolution element relative to the source of radiation is small enough such that the small angle approximation holds true, it should also hold that there is a one-to-one correspondence between intensity and flux. Thus, flux from a *single* source can be written simply as

$$\mathbf{F} = I(s_0)e^{-\tau(s)}\hat{\mathbf{n}} = \frac{L}{4\pi s^2}e^{-\tau(s)}\hat{\mathbf{n}}, \qquad (10)$$

where L is the luminosity of the source of radiation. The total flux is then computed by summing up flux contributions from all sources. For the remainder of paper we represent the radiation field as flux values computed via the above expression.

2.2   Algorithm

Please note that although TREVR has been initially implemented in the SPH code GASOLINE (Wadsley et al. 2004), TREVR is not specific to GASOLINE or SPH in general. The method only requires that the simulation volume is hierarchically partitioned in space and so it could be used directly in an adaptive mesh refinement (AMR) code.

The TREVR algorithm is based around a tree data structure which partitions the simulation volume hierarchically in space. The smallest resolution elements are or are contained by in the leaf nodes of the tree data structure. In Lagrangian or "particle" methods such as SPH, a number of SPH particles can be contained by a leaf node or "bucket". The maximum number of particles per bucket is referred to as N_B. In Eulerian or "grid" based methods the bucket is the smallest grid cell itself, so N_B is effectively one. N resolution elements hold radiation intensity values and represent the radiation field TREVR computes.

2.2.1   Source Merging

As mentioned in the introduction, a naïve algorithm would compute interactions between a resolution element and all sources of radiation. If we assume the number of resolution elements is equal to the number of sources, an infeasible number of interactions would need to be computed, scaling like $O\left(N^2\right)$. To mitigate this N^2 scaling TREVR employs source merging similar to particle merging in the Barnes & Hut (1986) tree-based gravity solver which has remained commonplace in astrophysical simulations (Benz 1988; Vine & Sigurdsson 1998; Springel et al. 2001; Wadsley et al. 2004; Hubber et al. 2011). Merging sources of radiation was first implemented in a rudimentary version of TREVR that did not consider extinction of any kind (Kannan et al. 2014). Sources of radiation are merged together at their centre of luminosity if they meet an "opening angle" criteria. This criteria is defined as

$$\theta_{\text{open}} > l/r, \qquad (11)$$

where l is the side length of a tree cell, r is the distance between the centre of luminosity of a source and centre of mass of a resolution element and θ_{open} is the opening angle, a fixed accuracy parameter. If a group of sources occupy the biggest tree cell that meets this criteria, all sources in that cell are merged into one, considerably reducing the number of interactions TREVR computes. This is illustrated in the left panel of Fig. 2, where the grey angle represents a cell whose angular size meets the opening angle criterion.

The cost savings of source merging can be quantified by integrating the number of tree cells that are "opened" according to the opening angle criteria. These opened cells will have their sources merged making them a single source. We will call the total count of the opened cells N_{open}. We can theoretically compute N_{open} this by integrating spherical shells of thickness dr along the path from a resolution element r, and then dividing the sphere volume by the volume of an opened cell, $V_{\text{open}}(r)$.

$$N_{\text{open}} = \int_{R_0}^{R} \frac{4\pi r^2}{V_{\text{open}}(r)} dr \qquad (12)$$

The bounds of the above integral go from R_0, the size of a bucket cell, to R, the length of the simulation volume. Because the number of particles in a simulation is proportional to the simulation volume, the lower integration limit can be expressed using particle numbers via

$$\frac{R_0}{R} = \sqrt[3]{\frac{N_B}{N}}, \qquad (13)$$

the cubed root of the ratio of the average number of particles per bucket, N_B, to the total number of simulation particles. Note that N_B (N_B = 10 for this paper) is only needed for particle methods. In a grid method a bucket is just the lowest level grid cell in the tree and $N_B = 1$. The opened cell volume can also be rewritten by cubing the opening angle criteria

$$V_{\text{open}}(r) = l^3 = \theta_{\text{open}}^3 r^3. \qquad (14)$$

Substituting gives us the following integral and its solution,

$$N_{\text{open}} = \int_{\left(\frac{N}{N_B}\right)^{-\frac{1}{3}}}^{R} \frac{4\pi r^2}{\theta_{\text{open}}^3} dr \sim \log N/N_B. \qquad (15)$$

This result means that the number of interactions scales like $O(N \log N)$. This is also the total cost scaling in the optically thin regime, which is unsurprising given the RT problem is almost identical to the gravity problem in the absence of intervening material. That brings up the next part of the algorithm, what to do about tracing a ray in the optically thick regime.

2.2.2   Tracing Rays

In the presence of absorbing material along a ray, the optical depth needs to be computed along said ray by computing the optical depth integral introduced in Eq. 7. To solve this integral numerically, we traverse the tree between the source and resolution element to build up the optical depth. This is possible because the tree partitions and fills space, thus all the intervening material should be contained in the tree we traverse. Making use of properties computed during the tree build, we can compute the optical depth of the i'th piece of
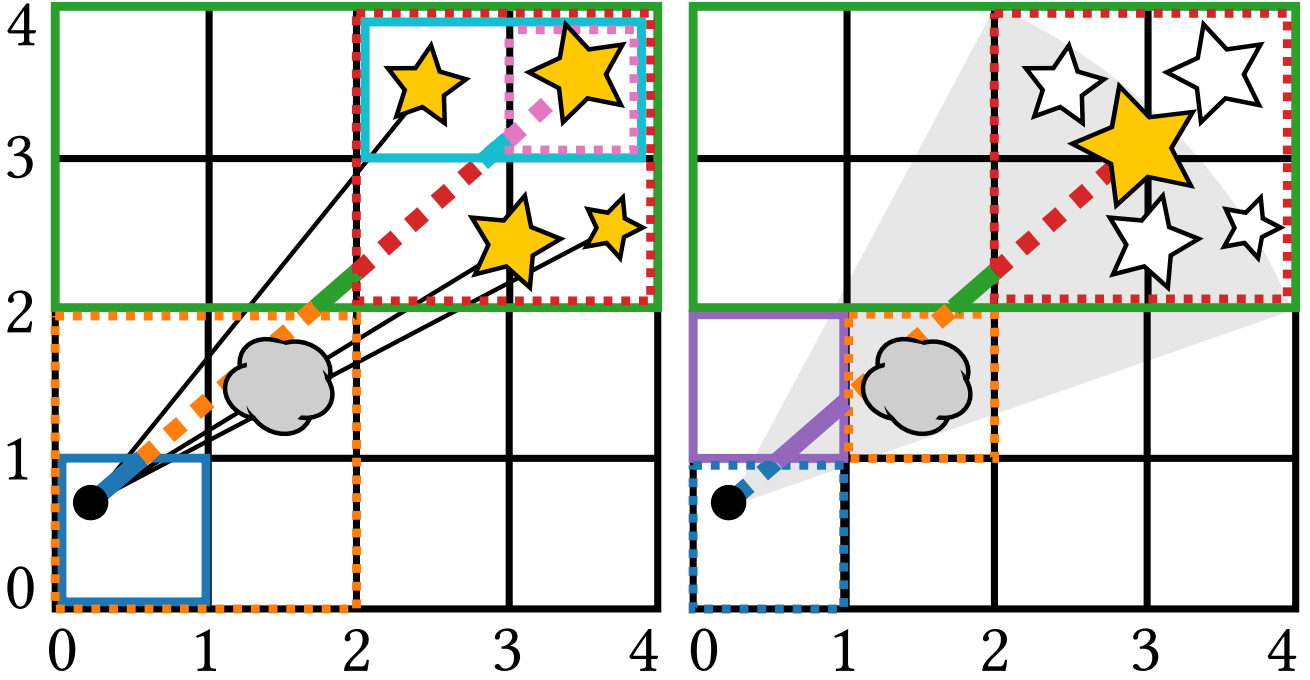
Figure 2. A schematic of TREVR without (left) and with source merging and adaptive refinement (right). Coloured ray segments correspond to tree cells whose average properties are used to compute the optical depth along said ray segment. Dashed and solid lines distinguish consecutive line segments to help associate them with their corresponding tree cell. The grey cloud represents a feature in the medium that requires refinement to be resolve. The smaller stars which are yellow in the left panel and white in the right panel represent individual radiation sources. The larger yellow star in the right panel represents a merged source, as the dashed red cell encapsulating all sources meets the opening angle (grey region in left panel) criteria.

the ray (τ_i) using the intersection length of the cell and ray (s_i) as well as the average density ($\bar{\rho}_i$) and average opacity ($\bar{\kappa}_i$) in the cell

$$\tau_i = \bar{\rho}_i \bar{\kappa}_i s_i. \qquad (16)$$

The total optical depth is then summed up during the tree walk,

$$\tau = \sum_i \tau_i, \qquad (17)$$

giving us everything needed to evaluate Equation 10.

This process is also illustrated in the left panel of Figure 2. In this figure ray segments and corresponding cells share the same colour. When referring to specific cell colours, they will also be identified by two sets of points [$(x, y), (x, y)$] corresponding to the bottom left and top right vertices of the cell respectively. Dotted lines are used to distinguish consecutive ray segments and help associate ray segments and their corresponding cells. In the left panel of Figure 2 there are two important things to note. Firstly, since we are performing a reverse ray trace, the resolution element denoted by the black circle is intrinsically well resolved at the bucket cell (the blue cell at at [$(0, 0), (1, 1)$]) level. However, the second point is that as the tree is walked upwards space becomes less resolved. It should be apparent that the central parts of the ray are less resolved (the green cell at [$(0, 2), (4, 4)$]) and as you move towards the source or resolution element the ray becomes more resolved (the red cell at [$(2, 2), (4, 4)$] and the

orange cell [$(0, 0), (2, 2)$]). This can be looked at in two ways. If the medium is uniform, the algorithm can be extremely efficient while still being able to resolve a sharp feature in the radiation field such as an ionization front. However, if the medium is highly irregular along the ray the algorithm will not be able to resolve sharp density and opacity gradients which could significantly alter the optical depth. Thus adaptive refinement is needed during the tree walk to accurately resolve the medium along the ray.

2.2.3 Adaptive Refinement

Consider the right panel in Figure 2. A dense blob of gas to be resolved resides in the orange highlighted cell at [$(1, 1), (2, 2)$]. At the point in the tree walk where we reach the orange highlighted cell at [$(0, 0), (2, 2)$] in the left panel, a decision needs to be made on whether the current cell sufficiently represents the media. This decision is made by a refinement criteria. If the cell passes the criteria to refine, rather than using its average properties we recursively check the cell's children until the criteria fails. Thus building a better resolved section of the ray.

Difficulty comes in choosing a refinement criteria that is both accurate and efficient. Ideally, the criteria should be true when an average optical depth in a region may not be accurate to the true distribution, such as a clumpy medium where the average density and opacity is much higher than the "effective" density and opacity (Városi & Dwek 1999;
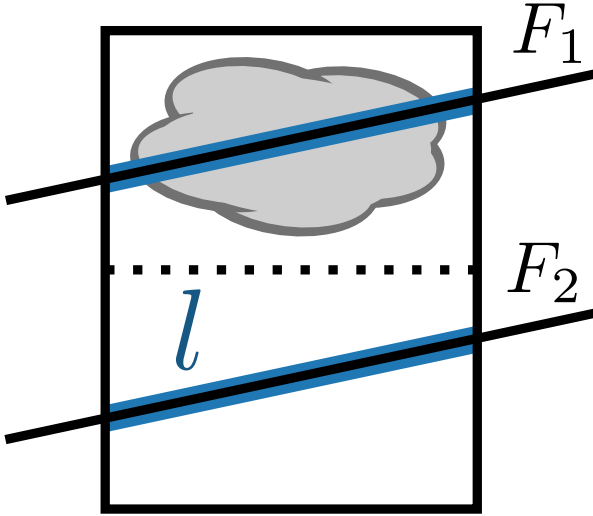
Figure 3. Schematic of a cell to be refined. A parent cell intersected by a ray contains a feature (grey cloud) to be resolved. The black dotted line partitions the parent cell into it's children. The black intersecting rays represent the hypothetical case where only a child cell is intersected by a ray. The blue outlined sections on each ray correspond to the intersection length, l, used to compute the optical depth through each child cell.

Hegmann & Kegel 2003). For this reason we have chosen an optical depth based refinement criteria that is unique to TREVR.

Consider two rays through through a large cell as in Figure 3. These rays represent what the case would be if properties of the children were used instead of the parent cell. We can compute the minimum and maximum absorption coefficients $\alpha_{\min}$ and $\alpha_{\max}$, via their minimum and maximum density and opacity values computed during the tree build. This multiplied by the intersection length l gives us the minimum and maximum optical depths, $\tau_{\min}$ and $\tau_{\max}$. We can then test the following refinement criteria

$$\tau_{\text{ref}} < \tau_{\max} - \tau_{\min}, \tag{18}$$

and refine if it is true. The fractional error in flux, per ray segment, for a chosen value of τ_{ref} is

$$\frac{F_1 - F_2}{F_1} \le 1 - e^{-\tau_{\max} - \tau_{\max}} \lesssim \tau_{\text{ref}}, \tag{19}$$

for small τ, making the refinement criteria a convenient choice of parameter for controlling error. Figure 9 is an example of TREVR's adaptive refinement in action.

If the refinement criteria passes at the bucket level, individual particles within a bucket are considered. A straight forward N^2 ray tracing scheme similar to SPHRay (Altay et al. 2008) can be performed on bucket particles and their neighbours. In the worst case where the refinement criteria passes the bucket level every time, a cost of $O(C_n N)$ is added to the scaling, where C_n is the constant number of SPH neighbours.

Fully characterizing the computational cost of the algorithm including the addition of adaptive refinement follows the same method as used earlier. However, now instead of in-

tegrating the number of sources we integrate the total number of ray segments computed. We will look at two cases, not refining at all and fully refining down to the bucket level. This will give us upper and lower bound for the algorithms scaling as characterizing the refinement between these extremes depends on the specific density and opacity distributions being operated on.

First let's consider the case where the refinement criteria always passes and all rays are resolved down to the bucket level. The number of segments per ray is then just the length of a ray divided by the size of a bucket. We can express this as

$$N_{\text{seg}} = \frac{r}{R_0} = \frac{r}{R}\left(\frac{N}{N_B}\right)^{\frac{1}{3}} \tag{20}$$

after substituting Eq. 13 in for R_0. Since N_{source} is also the number of rays computed, the total number of ray segments computed is just Eq. 12 multiplied by the number of ray segments

$$N_{\text{seg}} = \int_{\left(\frac{N}{N_B}\right)^{-\frac{1}{3}}}^{R} \frac{4\pi r^2}{\theta_{\text{open}}^3} \frac{r}{R}\left(\frac{N}{N_B}\right)^{\frac{1}{3}} dr \sim N(2N/N_B)^{\frac{1}{3}}. \tag{21}$$

This results means that the total cost of the algorithm scales like $O\left(N^{4/3}\right)$ in the worst case.

In the case were the refinement criteria never passes, the ray is split into segments made up of the cells traversed in the tree walk of the sub-tree going from source to resolution element. The number of cells traversed in a tree walk is equal to the logarithm of the number of leaf nodes contained within the sub-tree. The number of leaf nodes in the sub-tree is also given by Eq. 20, so by taking the logarithm of Eq.20 and adding two for the two buckets on either side of the sub-tree we come to

$$N_{\text{seg}} = \log_2\left[\frac{r}{R}\left(\frac{N}{N_B}\right)^{\frac{1}{3}}\right], \tag{22}$$

where the logarithm is base two as GASOLINE and thus TREVR is implemented using a binary tree. As before we multiply Eq. 12 by the number of ray segments and integrate the following

$$N_{\text{seg}} = \int_{\left(\frac{N}{N_B}\right)^{-\frac{1}{3}}}^{R} \frac{4\pi r^2}{\theta_{\text{open}}^3} \log_2\left[\frac{r}{R}\left(\frac{N}{N_B}\right)^{\frac{1}{3}}\right] dr \sim N\log^2(128N/N_B). \tag{23}$$

This results means that the total cost of the algorithm scales like $O\left(N\log^2 N\right)$ in the best case.

2.2.4 Background Radiation

In order to treat simulations properly we must account for the radiation coming from the rest of the universe outside of the simulation volume. Most current codes apply a constant UV field to the entire box, essentially the lowest order approximation possible. Some specialized codes like URCHIN (Altay & Theuns 2013) do a reverse ray trace to the edge of the box, where the background flux is assumed to be coming from. Others, such as TRAPHIC (Pawlik & Schaye 2008) allow their ray trace to be periodic. We believe that this periodic treatment is problematic. The cosmic UV radiation field originates from very large distances on the order of a
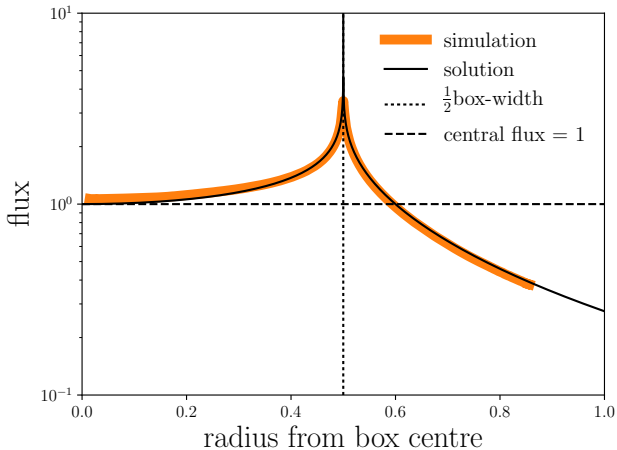
Figure 4. Flux as a function of radius from an emitting sphere. TREVR's solution for background source particles distributed in a spiral on a sphere of radius $R = 0.5$ (black dotted line) are plotted as the thick orange line. The analytical solution given by Equation 24 is plotted as a thinner black line on top of the numerical solution. A constant flux of one is plotted by the black dashed line and is achieved in the inner most region of this simulation at around $R \lesssim 0.05$

2.3 Implementation Specifics

As mentioned earlier, TREVR is not specific to either GASOLINE or SPH. However, in this subsection we would like to take the time to briefly introduce GASOLINE and the specifics of TREVR's implementation in GASOLINE.

GASOLINE is a parallel smoothed particle hydrodynamics code for computing hydrodynamics and self-gravity in astrophysics simulations. It employs a spatial binary tree that is built by recursively bisecting the longest axis of each cell. In the current version of TREVR, a separate tree is built for computing radiative transfer. For development this is a convenient choice, but adds extra cost and in the future a "one tree to rule them all" approach should be adopted. One of the main differences between these trees is that the radiation tree is required to fill all space. The main tree "squeezes" cell bounds to the furthest extents of a particle's influence. This does not work in the context of RT as cell and ray intersections need to be computed to sum up a correct optical depth along the entire ray.

In the regular tree building phase GASOLINE assigns an "opening radius" about a cells centre of mass to each cell in the tree. The specific definition of this radius is where B_{max} is the distance from the centre of mass of particles within the cell to the furthest particle from the centre of mass. However, since we are using space filling cells for the radiation tree it is necessary to define B_{max} as the distance to the furthest vertex of the cell instead of particle.
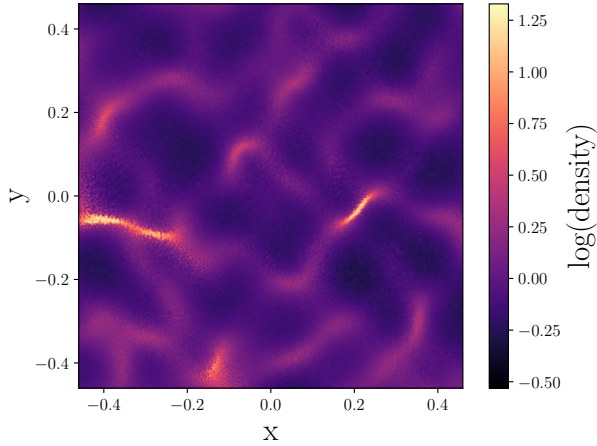
3 CODE TESTS

3.1 Sinusoidally Perturbed Glass
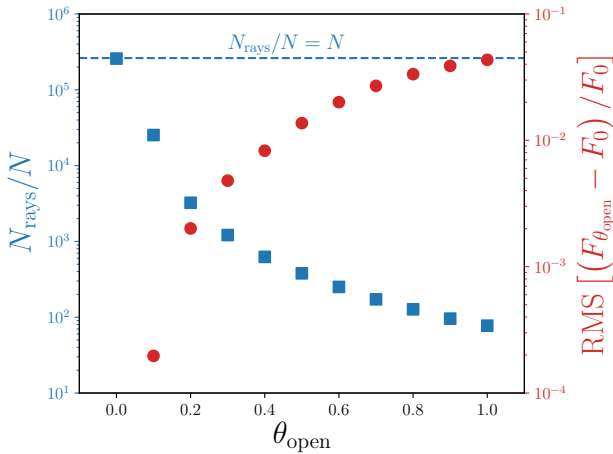
3.1.1 Initial Conditions

To test the accuracy and general scaling of the algorithm, an varying initial condition (IC) that the accuracy criterion can operate on while being representative of a typical use case is needed. For this we have created a novel IC comprised of a unit length glass of N SPH gas and N star particles whose positions have been perturbed by 24 random sinusoidal modes. The initial glass of particles comes from as 16^3 glass used to create initial conditions for other tests of GASOLINE (Wadsley et al. 2017). The total mass of gas particles is one, and the opacity of each particle is also one. This results in an optical depth across the width of the box of ~1, making the simulation volume optically thin overall with dense, optically thick filamentary structure and under-dense voids qualitatively similar to the cosmic web. Each star particle is also assigned a luminosity of one. A slice of this density distribution is plotted in Figure 5. Appendix A contains a detailed explanation of how this IC was created including a table of modes used.

3.1.2 Opening Angle

The opening angle criteria's affect on accuracy and cost was tested by simulating the optically thin, sinusoidally perturbed glass IC with θ_{open} varying between 0 and 1. The results of this test are plotted in Figure 6. The measure of cost is plotted as the total number of rays, N_{rays}, computed per resolution element on the left y-axis. The number of

gigaparsec. This is too large of a region to practically simulate, so radiation originating from periodicity is too local.

Instead, we have implemented a method involving tracing "background sources" similar to URCHIN. "Background" particles are distributed in a spiral pattern on the surface of a sphere at the very edge of the simulation volume (or at a large distance if required) and the number of sources can be varied to match the required angular resolution of the background. Finding the flux at the centre of a sphere of sources is a problem akin to Newton's Shell Theorem. However, because the intensity does not cancel like force, the solution differs and is as follows:

$$F(r) = \frac{L}{8\pi R} \ln\left(\frac{R+r}{R-r}\right), \qquad (24)$$

where L is the total luminosity of the emitting shell, R is the radius of the sphere and r is the radius the flux is being computed at. The shape of the function can be seen in Figure 4 where we have plotted the flux as a function of radius for a homogeneous, optically thin test volume.

Note that due to the logarithm in Equation 24, the flux is nearly constant at small radii. Since most cosmological zoom in simulations only consider gas at a fairly small radius, this setup of background sources is an acceptable method to provide a background flux. A benefit of this method is that we can use all of the existing machinery described in the methods section, and only have to add temporary background star particles as the source of the background radiation. Also not that the simulation flux is over estimated near the central region and underestimated at large radii. When merging background sources which are all located on the surface of a sphere, the merged centre of luminosity will always be at a smaller radius than that the sphere radius. This can be remedied by enforcing merged background sources to always be located on the sphere.

Figure 5. A z-plane slice of the sinusoidally perturbed glass IC. The optical depth along the longest filament in the slice (left, just below $y = 0$) is $\tau \approx 4$. The optical depth across the largest void (above the aforementioned filament) is $\tau \approx 0.1$.

Figure 6. A plot of cost and accuracy as a function of opening angle. The number of rays computed per resolution element is plotted on the blue, left axis with square markers. The blue dashed line points out $N_{\text{rays}}/N = N$ at an opening angle of $\theta_{\text{open}} = 0$, meaning TREVR can perform an $O\left(N^2\right)$ ray trace if desired (omitting the cost of absorption). The RMS error in flux relative to $\theta_{\text{open}} = 0$ is plotted on the red, right axis with circular markers.

rays is equivalent to the number of radiation sink-source interactions computed in a simulation time step. Using rays as a measure of cost allows us to separate the affects of the refinement criteria on cost. On the right y-axis, the root mean squared (RMS) fractional error relative to the radiation field computed with $\theta_{\text{open}} = 0$. A refinement criteria value of $\tau_{\text{ref}} = 0.1$ and $N = 64^3$ for both star and gas particles.

At $\theta_{\text{open}} = 0.75$, the value used in all other tests and the default value for θ_{open} in many gravity solvers, 200 rays are computed per resolution element with an RMS fractional error of 3%. To get to an RMS fractional error of about 1%,
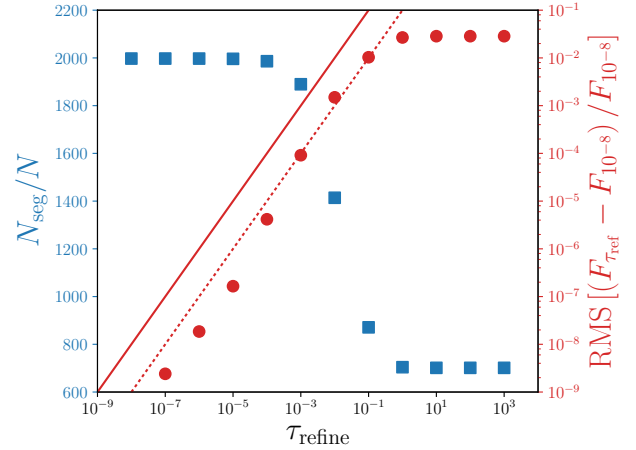
Figure 7. A plot of cost and accuracy as a function of refinement criteria. The number of ray segments computed per resolution element is plotted on the blue, left axis with square markers. The RMS error in flux relative to $\tau_{\text{ref}} = 10^{-8}$ is plotted on the red, right axis with circular markers. Lines of RMS $= \tau_{\text{ref}}$ and RMS $= \tau_{\text{ref}}/10$ are plotted as red solid and dotted lines respectively. The upper line represents in maximum allowable error *per ray segment*. The RMS relative error lies along or below the lower line, an order of magnitude less that than τ_{ref}.

a opening angle of $\theta_{\text{open}} = 0.45$ is needed and costs only 500 rays per resolution element. The cost at $\theta_{\text{open}} = 0.45$ is still much less than interacting with all 64^3 (2.6×10^5) sources, and could be a standard default value to move forward with.

3.1.3   Refinement Criteria

Testing the refinement criteria is similar to testing the opening angle criteria. Again, the sinusoidally perturbed glass IC was simulated but now with a varying τ_{ref} value. The results of this test are plotted in 7. The min and max values of τ_{ref} tested were chosen such that the cost curve flattens out on either side. The left hand side being where refinement has occurred down to the bucket level, and the right hand side end being where refinement is never done. A opening angle of 0.75 was used and $N = 64^3$ for both star and gas particles. Cost is plotted on the left y-axis and RMS fractional error on the right y-axis. The measure of cost is now number of ray segments per resolution element, since the refinement criteria controls how refined a ray becomes. The measure of accuracy is again the RMS fractional error, but now relative to the radiation field computed with $\tau_{\text{ref}} = 1 \times 10^{-8}$, the lowest τ_{ref} tested.

At $\tau_{\text{ref}} = 0.1$, 1% RMS fractional error is achieved with a cost of approximately 850 ray segments computed per resolution element, less than half the cost of refining all the way to the bucket level. Note also that RMS fractional error as a function of τ_{ref} behaves predictably, lying below the RMS $= \tau_{\text{ref}}$ line and roughly following the RMS $= \tau_{\text{ref}}/10$ line plotted in Figure 7. This in in agreement with our theoretical claim in Equation 19, that the maximum allowable error in flux per ray segment should be less than and proportional to τ_{ref} for small τ.

The RMS fractional error maxes out at 2-3% in this test.
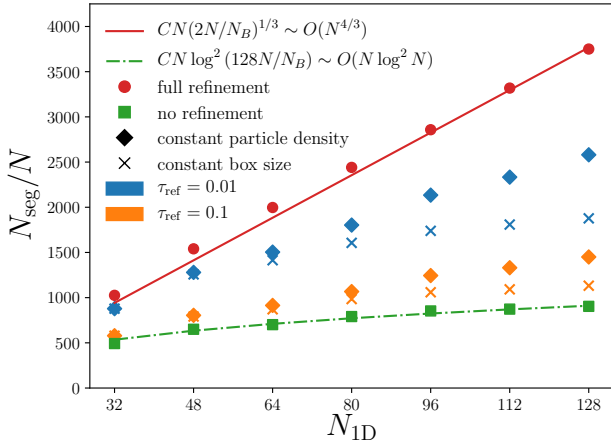
Figure 8. Cost, quantified as number of computed ray segments per resolution element, is plotted as a function of $N_{1D} = \sqrt[3]{N}$. TREVR's theoretical upper and lower scaling bounds are plotted as red (solid) and green (dash-dot) lines respectively. The corresponding simulation data points are plotted as red circles and green squares. Simulation data points intermediate to the scaling bounds are plotted as combinations of two parameters - refinement criteria value and the type of scaling. Test's run with a refinement criteria of $\tau_{ref} = 0.1$ are coloured orange and make up the lower two sets of intermediate data. The upper sets of intermediate data, coloured blue, are tests run with $\tau_{ref} = 0.01$. Diamond markers denote weak scaling tests and × shaped markers denote strong scaling tests.

In this particular implementation of TREVR, the walk along the ray goes up from both the bucket where the radiation sink resides and the opened cell where the source resides to the top of the tree. This built in level of refinement is the reason for the low maximum error. Other implementations, that walk the ray top down or up and then back down the tree, would need to rely more or solely on the refinement criteria. In principle, such a method could perform better than $O\left(N \log^2 N\right)$.

3.1.4 Scaling

To test cost scaling as a function of N, we hold θ_{open} constant at 0.75 and vary N between 32^3 and 128^3 in steps of $N_{1D} = 16$ for both gas and star particles. To substantiate our best and worst case theoretical scaling claims made in Equations 23 and 21 respectively, the sinusoidally perturbed glass IC was simulated with $\tau_{ref} = 1 \times 10^6$ to insure refinement was never performed and with $\tau_{ref} = 0$ to insure refinement was always performed down to the bucket level. Data from theses tests and fitted theoretical lines were plotted in Figure 8 and correspond very closely to each other. Note that the only parameter used to fit the theoretical lines from was a constant factor of C placed in front of Equations 21 and 23.

Scaling behavior between the upper and lower limits was probed in two ways. Firstly, simulations were run with τ_{ref} values of 0.1 and 0.01. Secondly, strong and weak scaling cases were simulated. The strong scaling case being where the simulation volume was held constant and particle number increased. This is analogous to increasing the resolution

of an isolated galaxy simulation. The weak scaling case is the opposite, where the box size is increased and particle density is held constant. This is analogous to simulating larger and larger cosmological boxes to achieve larger statistical samples. Note that the previously described tests of the upper and lower scaling bounds were run as strong scaling tests only.

Again, data from these tests was plotted in Figure 8 where there are two interesting things to note. Firstly, the strong scaling case, which is typically the harder case to scale well in, scales better than the weak scaling case. The strong scaling data turns over more similarly to the $N \log^2 N$ function and costs less than the weak scaling data. This is because unlike gravity, tracing a ray through intervening material will always cost more on longer length scales. Whereas in the strong scaling case, an increased number of particles represent the same density and opacity distribution and the refinement criteria will still act in the similar way, now with more particles per cell to average over. The second thing to note is that the strong scaling case at $\tau_{ref} = 0.1$, which achieved an RMS fractional error of 1% in the $N = 64^3$ sinusoidally perturbed glass test, scales similarly to the no refinement data and fit to $N \log^2 N$.

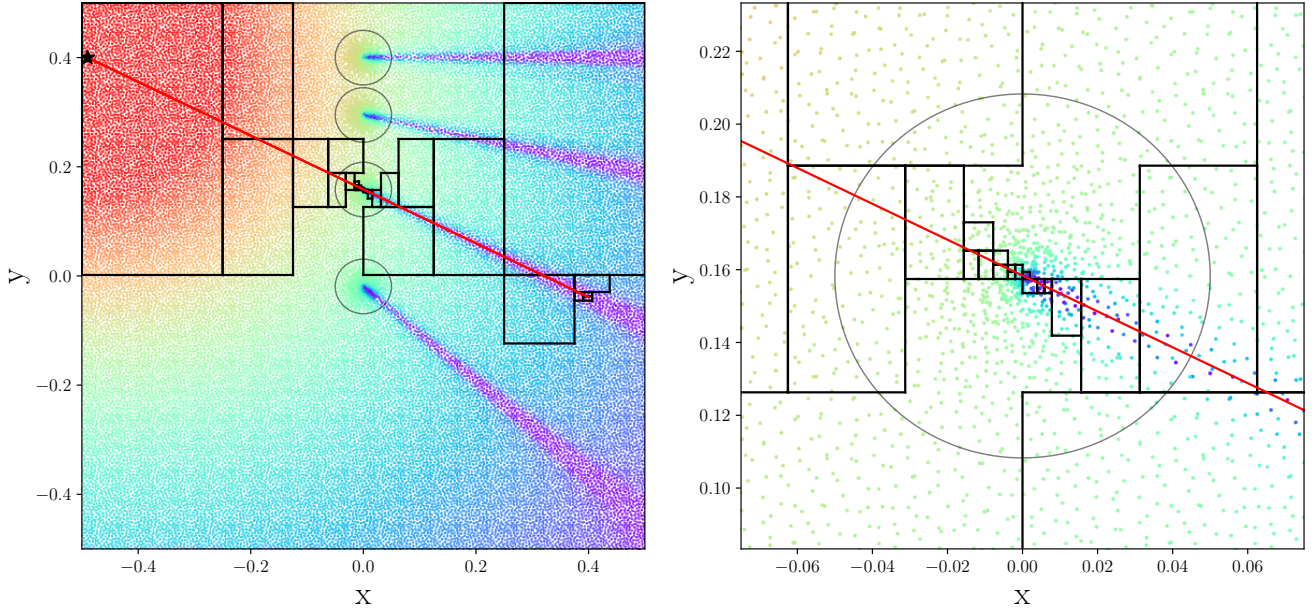### 3.2 Isothermal Spheres

3.2.1 Initial Conditions

The sinusoidally perturbed glass IC tested a generally optically thin, smooth density distribution. This is a good proxy for many astrophysical cases of interest, such as late stage galaxy evolution..As a test of how TREVR's refinement criteria can handle compact, optically thick features we created the Isothermal Spheres IC. This IC consists a single radiation source positioned in the top left corner and four spheres with $1/r^2$ density profiles embedded in a uniform glass. The spheres produce shadows down and to the right of the source. Accurate shadows can only be cast if the sharply peaked spheres are resolved correctly by the refinement criteria. Error specifically in the optically thick regime can be separated out by looking at only particles in shadow. The four isothermal spheres follow the density distribution described by

$$\rho(r) = \frac{\rho_0 \epsilon}{r^2 + \epsilon^2}, \tag{25}$$

where the softening length, ϵ, is 0.002 and the central density, ρ_0, is 626. The IC was made by adding SPH gas particles near the sphere centers using a stretched glass of. **Grond: James, could you fill this part in? I don't have the script you used to do this on hand.** These parameters set the maximum optical depth through a sphere to $\tau_{max} = 4$ (98% reduction in flux) and the density at the edge of the spheres to one, matching the unit density of the uniform background. The isothermal spheres have a radius of 0.05 and are denoted by the grey circles in Figure 9. They are centred on the x and z axis with y coordinates given by

$$y_i = 0.75 - 1.3^{-(4-i)}, \tag{26}$$

where i runs from zero to three. The radiation source, denoted by the black star in Figure 9, is located at $x = 0.49$, $y = y_0$ and $z = 0$. The total number of particles in the IC is $N = 4111624$.

Figure 9. Right: TREVR's adaptive refinement criteria resolving isothermal spheres in a uniform environment. Particles in a slice along the z-plane of the isothermal spheres IC are coloured by the logarithm of their flux value (high - low flux, red - purple). The red line represents the ray traced from radiation source (black star) to the receiving cell. Black rectangles represent the spatial boundary of the tree cells used compute the optical depth of the intersecting ray segment. Left: A zoom in of the sphere intersected by the ray to focus on the refinement across the sphere itself.

3.2.2 Refinement Criteria

The effects of the refinement criteria on accuracy and cost in this test were analyzed similarly to the data plotted for the Sinusoidally Perturbed glass IC test in Figure 7. The main addition to Figure 10 is the subset of particles in shadow has its RMS fractional error plotted separately to probe the refinement criteria's performance in the optically thick regime. Again, $\tau_{\rm ref} = 0.1$ achieves an RMS fractional error of 1% with very little cost. However, when only considering particles in shadow the same refinement criteria produces almost an order of magnitude more error at about 8%. Decreasing the refinement criteria by an order of magnitude to $\tau_{\rm ref} = 0.01$ predictably decreases the RMS fractional error on particles in shadow to 1% with a negligible cost increase from $\tau_{\rm ref} = 0.1$.

The RMS = $\tau_{\rm ref}$ and RMS = $\tau_{\rm ref}/10$ lines are again plotted in Figure 10. For the most part the RMS fractional error is contained between these lines, with only two of the in-shadow points at $\tau_{\rm ref} = 1 \times 10^{-5}$ and 1×10^{-4}, and one of the all particle points at $\tau_{\rm ref} = 1 \times 10^{-4}$ sitting ever so slightly above the RMS = $\tau_{\rm ref}$ line. Again, but now in a more difficult test when compared to the sinusoidally perturbed glass IC, Equation 19 proves to accurate in predicting that the maximum allowable error in flux per ray segment should be less than and proportional to $\tau_{\rm ref}$ despite only technically being valid for small τ. In most cases we believe TREVR should perform better as Equation 19 is just a reliable upper bound.

Wadsley: What about work we did for absolute errors? I'd like at least a comment with quantitative error numbers and preferably a plot too. Grond: I'll make this for my thesis ASAP and put it here after.
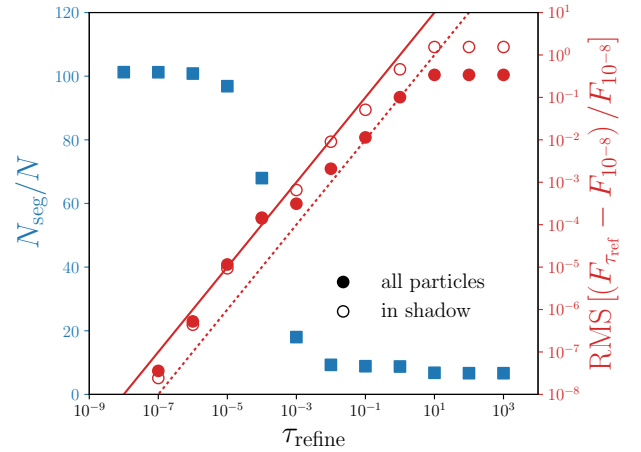
Figure 10. A plot of cost and accuracy as a function of refinement criteria. The number of ray segments computed per resolution element is plotted on the blue, left axis with square markers. The RMS error in flux relative to $\tau_{\rm ref} = 10^{-8}$ is plotted on the red, right axis with circular markers. Lines of RMS = $\tau_{\rm ref}$ and RMS = $\tau_{\rm ref}/10$ are plotted as red solid and dotted lines respectively. Solid circular markers represent RMS relative errors computed on all resolution elements and empty markers represent only the resolution elements that fall in the shadow of the isothermal spheres. The in shadow errors match closely with the all particle points on the RMS = $\tau_{\rm ref}$ line until the all particle points begin to diverge back onto the RMS = $\tau_{\rm ref}/10$ line (where they lay in Figure 7) at $\tau_{\rm ref} = 10^{-3}$.

3.3 Strömgren Sphere Test

3.3.1 Strömgren Sphere Theory

The Strömgren sphere is a theoretical ionized sphere of gas first discussed by Bengt Strömgren in 1938 (Strömgren 1939) as a model of regions around hot, young stars. The theoretical initial conditions consist of a cloud neutral hydrogen gas with an ionizing source of radiation at its centre. As photons from the source ionize the hydrogen, the optical depth of the gas decreases and so the ionizing photons are able to travel further and further from the source creating an ionization front. As the front moves radially outward from the source a radius is reached where the ionization rate equals the recombination rate. At this point, the front reaches equilibrium and stops creating a stable sphere of ionized hydrogen. The Strömgren sphere test has become a common code test in RT methods papers (Pawlik & Schaye 2008, 2011; Petkova & Springel 2011) and comparison papers (Iliev et al. 2006, 2009), as it it is a simple test of a method's ability to resolve ionization fronts and achieve equilibrium behaviour.

The equilibrium radius or Strömgren radius, R_S, is the radius at which the ionization and recombination rates are equal. This radius can be solved for by setting the two rates equal producing (e.g. Tielens 2005)

$$R_S = \left(\frac{3}{4\pi} \frac{\dot{N}_\gamma}{\alpha n_H^2} \right)^{1/3}, \tag{27}$$

where $\dot{N}_\gamma$ is the source luminosity in photons per second, α is the recombination rate and n_H^2 is the hydrogen number density. One can also solve for the radius as a function of time (e.g. Spitzer 1978),

$$R(t) = R_S \left[1 - \exp\left(t/t_{\text{rec}}\right) \right]^{1/3} \tag{28}$$

where $t_{\text{rec}=1/n_H\alpha}$ is the recombination time of the gas. The above derivation assumes a "sharp" ionization front, meaning the transition from ionized to neutral hydrogen is across an infinitesimally small region. In practice, the transition region is small compared to the size of the ionized region, but there is structure interior to the Strömgren radius that is not accounted for by simply solving for the equilibrium radius. In order to solve for the non-sharp ionization front we must consider the hydrogen ionization equation

$$\frac{\partial n_{\text{HII}}}{\partial t} = c\sigma n_{\text{HI}} n_\gamma - \alpha n_e n_{\text{HII}}, \tag{29}$$

where n_x is the number density of species x, HI and HII are neutral and ionized hydrogen respectively, γ is photons, σ is the ionization cross section, c is the speed of light and α is the recombination rate. Note that we have omitted collisional ionization in Equation 29 as it is not included in further testing, however it should be included in general. By integrating the ionization equation and the flux equation with absorption (Equation 10), we get a solution for HI/HII as a function of radius and as a function of time (Osterbrock & Ferland 2006). In the following tests, we include both theoretical sharp front solution and non-sharp front solutions from the Iliev et al. (2006) comparison paper to compare to our results as well as mimicking their initial conditions.
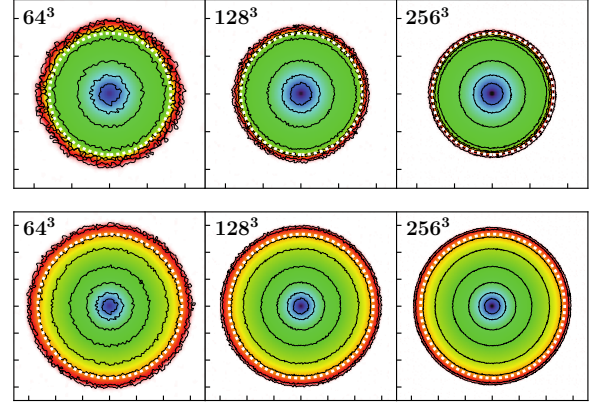
Figure 11. A slice through the z-plane of the isothermal Strömgren sphere test at $t = 30$ Myr (top row) and $t = 500$ Myr (bottom row). Particle resolutions increase from left to right denoted by the N value in the top left corner of each pane. Axis ticks are spaced 2 kpc apart, so note that ionized spheres in the top row are a fraction of the volume and particle resolution of spheres in the bottom row. The colormap represents neutral fraction, x and is similar to that of Pawlik & Schaye (2008) and Pawlik & Schaye (2011) for comparison. Also made identical for comparison are contour levels at x = 0.9, 0.5, log x = -1, -1.5, -2, -2.5, -3 and -3.5. The white dashed line is a circle of radius given by Equation 28, the sharp, time dependent solution to the isothermal Strömgren sphere.

3.3.2 The Isothermal Strömgren Sphere

In the simplest case, the ionizing source is assumed to emit monochromatic photons at 13.6 eV, meaning the gas is ionized but not heated. The gas is not allowed to cool, meaning the gas is isothermal. For this reason we will refer to this case as the Isothermal Strömgren Sphere. The medium is initially neutral with a temperature of $T = 10^4$ K and a density of $n_{\text{HI}} = 10^{-3}$ cm^{-3}. An ionizing source is turned on at $t = 0$ and emits at a rate of $\dot{N}_\gamma = 5 \times 10^{48}$ photons s^{-1}. We use an ionization cross section of $\sigma = 6.3 \times 10^{-18}$ cm^{-2} and a recombination rate of $\alpha = 2.59 \times 10^{-13}$ cm^{-3} s^{-1}, typical of 10^4 K gas. These values yield a Strömgren radius of $R_S = 5.38$ kpc and a recombination time of $t_{rec} \approx 125$ Myr.

We note that Iliev et al. (2006) uses a 6.6 kpc cube which only contains a single quadrant of the Strömgrensphere for their testing. We have opted to use an 16 kpc cube, increasing the maximum front radius to 8 kpc to avoid any edge effects, as the sphere gets close to the edge of the box for some codes in their paper. In order to aid comparison, we still normalize radius values to 6.6 kpc, as is done in Iliev et al. (2006). As well, we have not imposed a floor on the HII fraction of 0.001, as has been done in their paper. As the resolution used in the Iliev et al. (2006) comparison paper was never specifically given, we have opted to run the test with $N = 64^3$, 128^3 and 256^3 particles to represent the *entire* sphere. These resolutions correspond to single quadrant resolutions of $N = 32^3$, 64^3 and 128^3 in Iliev et al. (2006). Varying the number of particles also allows us to have a look at how TREVR converges with resolution. We have run our Strömgren sphere tests with fixed accuracy parameters of $\theta_{\text{open}} = 0.75$, $\tau_{\text{ref}} = 0.1$.

Figure 11 is a slice through the z-plane of the simula-

tion. The colour map corresponds to neutral fraction. The contour levels and colour map have been chosen to closely mimick Figure 6 in both Pawlik & Schaye (2008) and Pawlik & Schaye (2011). We have done this to highlight a main benefit ray tracers like TREVR have over photon packet propagation methods such as TRAPHIC - isotropy. At the same $N = 64^3$ particle resolution TREVR is more isotropically symmetric than TRAPHIC, even with their use of monte-carlo resampling. Furthermore, TREVR outperforms TRAPHIC in this aspect even at early times (top panels in Figure 11). Here the interior of the Strömgren sphere is represented by 3.3 times fewer particles than late time spheres in equilibrium plotted in the TRAPHIC papers (in this paper these are in the top panels of Figure 11).

Figure 12 is a plot of neutral/ionization fraction as a function radius from the Strömgren sphere centre. The sharp Strömgren radius is plotted as well as non-sharp solutions from all codes presented in Figure 8 of Iliev et al. (2006). TREVR tends to over-ionize at lower resolutions, but recreates the ionization profile quite well overall. At 30 Myr we converge with resolution to the sharp solution. At 500 Myr we converge to the non-sharp numerical solutions, which also over-ionize relative to the sharp solution at late times. Overall, the two higher resolution solutions are within the scatter of the non-sharp solutions of the codes presented in Iliev et al. (2006). It is interesting to not that the magnitude of over-ionization is related to resolution. We suspect the cause of over-ionization is **Grond: What exactly do we want to say here?**.

3.3.3 The Non-Isothermal Strömgren Sphere

The above test assumed the hydrogen gas was isothermal and that all incident photons had the same energy. In reality, photons range across many wavelengths with differing cross-sections at each wavelength. As well, absorption typically causes heating, which effects among many gas properties, recombination rate.

We rerun the Strömgrensphere test, but this time the incident photons are assumed to be from a black body with temperature 10^5 K. The cross section is now an integrated cross section, obtained by integrating the cross section as a function of wavelength between 13.6 eV and 29.65 eV, which gives $\sigma = 1.63 \times 10^{-18}$ cm^{-2}. The gas has an initial temperature of 100 K and the recombination rate is a function of temperature set by

$$\alpha(T) = 2.59 \times 10^{-13} \left(\frac{T}{10^4 \ K} \right)^{-0.7} \ cm^{-3} \ s^{-1} \quad (30)$$

to match Petkova & Springel (2009). This test includes heating due to absorption and cooling due to recombination Δ_r, collisional ionization Δ_{ci}, line cooling δ_l and Bremsstrahlung radiation Δ_B. The rates are taken from Cen (1992) in order to match Petkova & Springel (2009).

Figures 13 and 14 show the neutral/ionized fraction and temperature respectively as a function of radius at $t = 10$, 100 and 500 Myr. These times represent the fast expansion stage, slowing down stage and final Strömgren sphere respectively. We have plotted numerical solutions from Figures 16 and 17 in Iliev et al. (2006) for comparison. Again, TREVR recreates these profiles quite well in a qualitative sense. However, TREVR over-ionizes relative to all other

solutions at every resolution. We believe this is not caused by the TREVR algorithm specifically, as the isothermal test converged with resolution. It could possibly be a result of the ionization code and should be addressed in the future **Grond: Again, exactly what do we want to say here?**. On the other hand, the temperature profile lies in the middle of the scatter of the Iliev et al. (2006) solutions.

4 DISCUSSION AND CONCLUSIONS

Best practices

- what parameters do we suggest based on testing? What one should be careful about.
- specific things we will do wrong?

now we have this we can do these things
Our Niche

- why are isolated galaxy simulations best right now
- use in small scale, low source stuff?
- reionization is bad
- challenges for the cosmological box use case

Future Work

- How to deal with periodicity
- How to deal with finite speed of light (look back)
- More optimizations (turning off sources, when to stop tracing a ray)
- Complex source problem, why it might not be so bad

General Wrap Up

- Hammer out main points we want to end on (maybe in a list)

strict time step
- problem with cosmology (regions of space that generate UV field are enormous Gpc, add in background by hand) - scaling stuff is not specific to gasoline NB=1 - pp (explain it more in context of gasoline) - cosmo background (stuff merged on sphere)
32*3*N (more hops, resampling)
gasoline has multiple trees (3 trees), future work -> one tree to rule them factor of 3
int gasoline section (like sph ray?? how exactly)
For discussion should talk about how this (iso spheres) is hard test – single source. In more general case if goal is radiation field for chemistry or similar errors will tend to cancel in rms
Discussion: Traffic
~32 (N+Nvip) packets - 64 N packet hops per substep – often more even with reduced speed of light b/c must cover c x dt (I think Rahmati gave large multiplier) Will be of order c_{light}/c_{sound} Can't really win by doing fewer RT step since just increases the substep required Us ~1000 $N_{sink-active}$ ~10 N per substep, no subcycling needed because on average $N_{sink-active} \sim 1/100$ N
Discussion should include possible future improvements
Note: Healpix doesn't change order! $6N \rightarrow N$
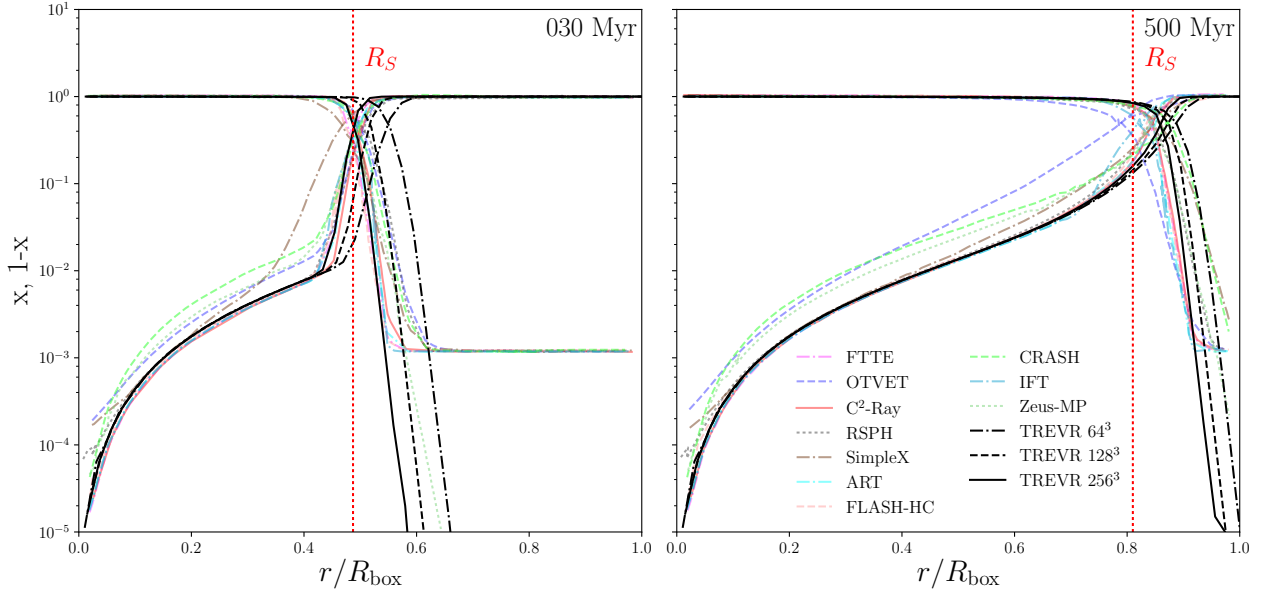
Figure 12. Spherically averaged neutral, x, and ionized, 1 − x, fraction profiles for the isothermal Strömgrensphere test during the fast expansion (left) and equilibrium (right) stages. Radius on the *x*-axis is normalised by a box length of 6.6 kpc for comparison with plotted solutions from the Iliev et al. (2006) comparison paper.
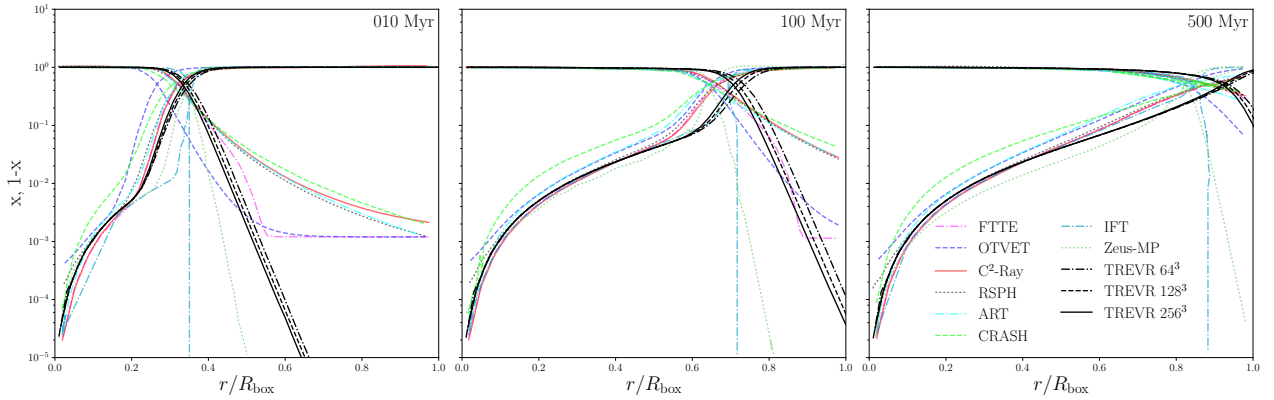
Figure 13. Spherically averaged neutral, x, and ionized, 1 − x, fraction profiles for the non-isothermal Strömgrensphere test during the fast expansion (left), slowing down (middle) and equilibrium (right) stages.
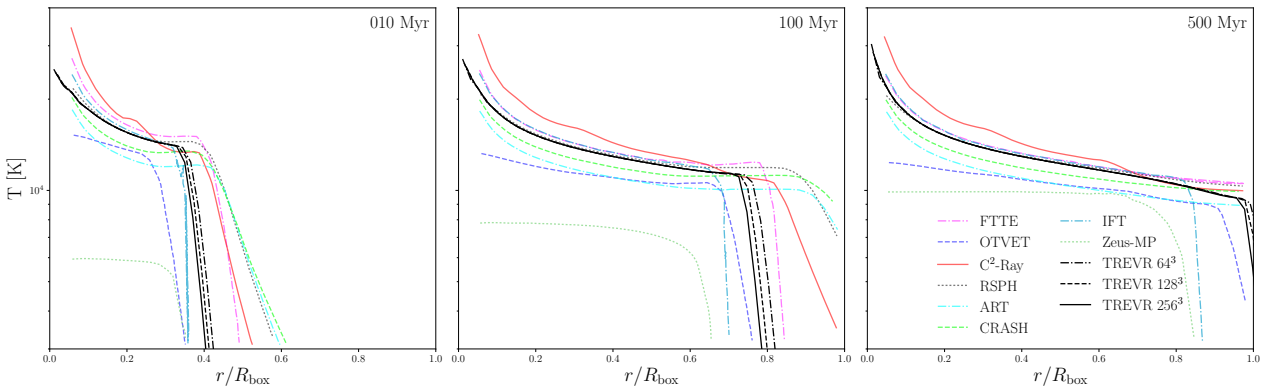
Figure 14. Spherically averaged temperature profiles for the non-isothermal Strömgrensphere test.

ACKNOWLEDGEMENTS

REFERENCES

Agertz O., Kravtsov A. V., Leitner S. N., Gnedin N. Y., 2013, ApJ, 770, 25
Altay G., Theuns T., 2013, MNRAS, 434, 748
Altay G., Croft R. A. C., Pelupessy I., 2008, MNRAS, 386, 1931
Baczynski C., Glover S. C. O., Klessen R. S., 2015, MNRAS, 454, 380
Barnes J., Hut P., 1986, Nature, 324, 446
Benz W., 1988, Computer Physics Communications, 48, 97
Cen R., 1992, ApJS, 78, 341
Chabrier G., 2003, PASP, 115, 763
Clark P. C., Glover S. C. O., Klessen R. S., 2012, MNRAS, 420, 745
Dale J. E., Ercolano B., Bonnell I. A., 2012, MNRAS, 424, 377
Gnedin N. Y., Abel T., 2001, New Astron., 6, 437
Górski K. M., Hivon E., Banday A. J., Wandelt B. D., Hansen F. K., Reinecke M., Bartelmann M., 2005, ApJ, 622, 759
Gritschneder M., Naab T., Walch S., Burkert A., Heitsch F., 2009, ApJ, 694, L26
Hegmann M., Kegel W. H., 2003, MNRAS, 342, 453
Howard C. S., Pudritz R. E., Harris W. E., 2016, MNRAS, 461, 2953
Howard C. S., Pudritz R. E., Harris W. E., 2017, MNRAS, 470, 3346
Hubber D. A., Batty C. P., McLeod A., Whitworth A. P., 2011, A&A, 529, A27
Iliev I. T., et al., 2006, MNRAS, 371, 1057
Iliev I. T., et al., 2009, MNRAS, 400, 1283
Kannan R., et al., 2014, MNRAS, 437, 2882
Leitherer C., et al., 1999, ApJS, 123, 3
Levermore C. D., Pomraning G. C., 1981, ApJ, 248, 321
Mellema G., Iliev I. T., Alvarez M. A., Shapiro P. R., 2006, New Astron., 11, 374
Mihalas D., Mihalas B. W., 1984, Foundations of radiation hydrodynamics. Courier Corporation
Osterbrock D. E., Ferland G. J., 2006, Astrophysics of gaseous nebulae and active galactic nuclei
Paardekooper J.-P., Kruip C. J. H., Icke V., 2010, A&A, 515, A79
Pawlik A. H., Schaye J., 2008, MNRAS, 389, 651
Pawlik A. H., Schaye J., 2011, MNRAS, 412, 1943
Petkova M., Springel V., 2009, MNRAS, 396, 1383
Petkova M., Springel V., 2011, MNRAS, 415, 3731
Rosdahl J., Teyssier R., 2015, MNRAS, 449, 4380
Spitzer L., 1978, Physical processes in the interstellar medium
Springel V., Yoshida N., White S. D. M., 2001, New Astron., 6, 79
Strömgren B., 1939, ApJ, 89, 526
Tielens A. G. G. M., 2005, The Physics and Chemistry of the Interstellar Medium
Városi F., Dwek E., 1999, ApJ, 523, 265
Vine S., Sigurdsson S., 1998, MNRAS, 295, 475
Wadsley J. W., Stadel J., Quinn T., 2004, New Astron., 9, 137
Wadsley J. W., Keller B. W., Quinn T. R., 2017, MNRAS, 471, 2357
Walch S. K., Whitworth A. P., Bisbas T., Wünsch R., Hubber D., 2012, MNRAS, 427, 625
Wise J. H., Abel T., 2011, MNRAS, 414, 3458

APPENDIX A: TEST INITIAL CONDITIONS

A1 Sinusoidally Perturbed Glass

To create our gently varying density distribution for the sink/source scaling tests, we modify positions of particles in

Table A1. Randomly generated $\vec{k}$ and ϕ values used in generating a gently varying density distribution.

i	$k_{x,i}$	$k_{y,i}$	$k_{z,i}$	ϕ_i
01	−3.918398	+1.727743	−4.476095	0.829776
02	−3.681821	−4.619688	+4.865007	3.891157
03	−4.831801	+3.769470	+0.567451	3.668730
04	−2.298279	+1.501757	+4.716946	1.528348
05	−0.289974	−3.097958	+1.270028	4.113001
06	+1.262943	−1.661726	−2.600413	4.481799
07	+1.588224	+4.072259	+0.616444	2.971965
08	−2.253394	−2.806478	+2.749155	0.442241
09	−1.432569	+3.324710	+4.842991	2.871989
10	+1.287742	−4.575517	−4.001723	1.727810
11	+4.769704	+0.540096	−4.203839	5.872117
12	−3.013200	−1.871251	−2.514416	1.574008
13	−4.588620	+4.384224	+1.246849	1.985715
14	−0.372817	+0.195243	+4.074056	6.248739
15	−1.842232	+0.901598	−4.453613	6.273336
16	+1.986937	−1.037650	+1.958888	2.177783
17	−1.748485	−1.386029	+3.755833	0.532604
18	+4.852406	−3.272506	+0.826504	5.525470
19	+3.663293	−4.597598	−0.890135	4.528870
20	−1.720903	+2.726011	+3.192427	3.875610
21	+4.973332	+4.777182	−2.515792	0.406737
22	+0.057238	−2.972427	−1.828550	4.125258
23	+0.938234	−0.487023	−2.755097	1.335299
24	+1.943361	+0.388178	−3.783953	4.774938

a glass initial condition by adding the sum of 24 sinusoidal modes as in equation A1 below

$$\vec{r} = \vec{r}_0 + \sum_{i=1}^{24} \frac{1}{275} \sin\left(k_{x,i} r_x + k_{y,i} r_y + k_{z,i} r_z + \phi_i\right), \quad \text{(A1)}$$

where $\vec{r}_0$ is the particles initial position in the glass and $\vec{r}$ is its perturbed position in the final distribution. The $\vec{k}_i$ and ϕ_i values are listed in table A1 for if one wishes to reproduce the scaling tests. Both gas and star particles have the same density distribution. However, the initial glass was flipped for the star particles by reassigning x, y and z coordinates via

$$x_{\text{star}} = y_{\text{gas}}, \quad y_{\text{star}} = z_{\text{gas}}, \quad z_{\text{star}} = x_{\text{gas}}, \quad \text{(A2)}$$

to prevent the particles from occupying the same position in space.

This paper has been typeset from a TEX/LATEX file prepared by the author.